

This is the accepted manuscript made available via CHORUS. The article has been published as:

K^{\ast} vector meson resonance dynamics in heavy-ion collisions

Andrej Ilner, Daniel Cabrera, Christina Markert, and Elena Bratkovskaya

Phys. Rev. C **95**, 014903 — Published 12 January 2017

DOI: [10.1103/PhysRevC.95.014903](https://doi.org/10.1103/PhysRevC.95.014903)

K^* vector meson resonance dynamics in heavy-ion collisions

Andrej Ilner,^{1,2,*} Daniel Cabrera,^{3,2,†} Christina Markert,^{4,‡} and Elena Bratkovskaya^{1,5,§}

¹*Institut für Theoretische Physik, Johann Wolfgang Goethe-Universität
Frankfurt am Main, 60438 Frankfurt am Main, Germany*

²*Frankfurt Institute for Advanced Studies (FIAS), 60438 Frankfurt am Main, Germany*

³*Instituto de Física Corpuscular (IFIC), Centro Mixto Universidad de Valencia - CSIC,
Institutos de Investigación de Paterna, Ap. Correos 22085, E-46071 Valencia, Spain.*

⁴*The University of Texas at Austin, Physics Department, Austin, Texas, USA*

⁵*GSI Helmholtzzentrum für Schwerionenforschung GmbH Planckstrasse 1, 64291 Darmstadt, Germany*

We study the strange vector meson (K^*, \bar{K}^*) dynamics in relativistic heavy-ion collisions based on the microscopic Parton-Hadron-String Dynamics (PHSD) transport approach which incorporates partonic and hadronic degrees-of-freedom, a phase transition from hadronic to partonic matter - Quark-Gluon-Plasma (QGP) - and a dynamical hadronization of quarks and antiquarks as well as final hadronic interactions. We investigate the role of in-medium effects on the K^*, \bar{K}^* meson dynamics by employing Breit-Wigner spectral functions for the K^* s with self-energies obtained from a self-consistent coupled-channel G-matrix approach. Furthermore, we confront the PHSD calculations with experimental data for p+p, Cu+Cu and Au+Au collisions at energies up to $\sqrt{s_{NN}} = 200$ GeV. Our analysis shows that at relativistic energies most of the final K^* s (observed experimentally) are produced during the late hadronic phase, dominantly by the $K + \pi \rightarrow K^*$ channel, such that the fraction of the K^* s from the QGP is small and can hardly be reconstructed from the final observables. The influence of the in-medium effects on the K^* dynamics at RHIC energies is rather modest due to their dominant production at low baryon densities (but high meson densities), however, it increases with decreasing beam energy. Moreover, we find that the additional cut on the invariant mass region of the K^* further influences the shape and the height of the final spectra. This imposes severe constraints on the interpretation of the experimental results.

PACS numbers:

I. INTRODUCTION

Heavy-ion collisions (HIC) at high energies are studied both experimentally and theoretically to obtain information about the properties of dense and hot matter since in the hadronic phase the quarks are confined to a colour-neutral state, whereas at high densities and temperatures the partons can move freely over larger distances (i.e. larger than the size of a hadron), which implies that the partons are deconfined and a new stage of matter - denoted as Quark-Gluon-Plasma (QGP)- is reached. Such extreme conditions were present shortly after the creation of the Universe and nowadays can be realized in the laboratory by heavy-ion collisions at relativistic energies. Indeed, in the last decade the QGP has been produced in a sizeable volume in ultra-relativistic heavy-ion collisions at the Relativistic Heavy-Ion Collider (RHIC) at the Brookhaven National Laboratory (BNL) and at the Large Hadron Collider at the Conseil Européen pour la Recherche Nucléaire (CERN) for a few fm/c after the initial impact of the collision.

Unlike early predictions that assumed a weakly interacting system of massless partons (parton gas),

which might be described by pQCD (perturbative Quantum-Chromo-Dynamics), experimental observations of Au+Au collisions at RHIC [1] have shown clear signatures of a new medium that is more strongly interacting than in the hadronic phase and behaves approximately close to an 'ideal' liquid. In order to study the properties of such QGP matter one looks for probes which provide information about the initial partonic stage. In the experiment only the final hadrons, leptons and photons are measured. In spite that electromagnetic probes allow to penetrate directly to all stages of heavy-ion collisions, they are very rare and it is quite complicated to identify the QGP signal among many other production channels of hadronic origin [2]. On the other hand, hadronic observables are more abundant and easier to access experimentally.

Apart from heavy hadrons with 'charm' [3] also strange vector-meson resonances K^*, \bar{K}^* s are considered as sensitive probes for the hot and dense medium [4, 5]. At relativistic energies the K^* s are generally expected to be produced at the partonic freeze-out (or even earlier [6]) and, thus, to provide information about the QGP stage close to hadronization. Accordingly, detailed studies of the K^* resonances have been performed by the STAR Collaboration at RHIC in the last decade [7–10]. Since the strange vector-mesons K^*, \bar{K}^* s are relatively short living resonances, dominantly decaying to pions and kaons ($K^* \rightarrow K + \pi$), it is difficult to reconstruct them experimentally since the pions and kaons suffer from final state interactions with other mesons and baryons in the ex-

*Electronic address: ilner@fias.uni-frankfurt.de

†Electronic address: cabrera@fias.uni-frankfurt.de

‡Electronic address: cmarkert@physics.utexas.edu

§Electronic address: E.Bratkovskaya@gsi.de

panding hadronic phase, i.e. the latter can rescatter or be absorbed. Moreover, the recreation of the K^* by fusion of a kaon and pion ($K + \pi \rightarrow K^*$) might 'over-shine' the K^* signal from the QGP and lead to additional complications. As known from chiral models or coupled-channel G-matrix approaches [12–17], the K^* resonances change their properties in a hot and dense hadronic medium and also the properties of the 'daughter' kaons/antikaons are affected by hadronic in-medium modifications [18]. All these effects should be accounted for when addressing or modelling the K^* production in relativistic HICs.

In order to interpret the experimental results [7–10] it is mandatory to study the dynamics of the K^* s within a proper theoretical framework. Statistical or hydrodynamic models can be used to obtain information on the bulk properties of the medium, however, to properly investigate the interactions of the K^* with the hadronic medium one needs a non-equilibrium transport approach to study the influence of the medium on the K^* and vice versa. Furthermore, one needs a consistent theory for the in-medium effects of the K^* as a function of the nuclear baryon density in order to trace the dynamics of the K^* during the later stages of the collision in the expansion of the hadronic fireball in close analogy to the kaon and antikaon dynamics in heavy-ion reactions at lower energies [19].

Previously there have been several studies on the strange vector-meson resonances K^* within different transport models at relativistic energies. In Refs. [20, 21] detailed calculations for Pb+Pb at $\sqrt{s_{NN}} = 17.3$ GeV have been performed using the cascade model UrQMD and it was found that the observability of strange particle resonances is distorted due to the rescattering of the strongly interacting decay products. Furthermore, the rescattering rate changes with rapidity and transverse momentum p_T of the reconstructed resonances, which leads to higher apparent temperatures for these resonances due to a sizeable depletion at low p_T which is most pronounced at midrapidity. Since the rescattering increases with baryon density, most resonances that can be reconstructed come from the low nuclear baryon density region. The authors of Ref. [22] used EPOS3 (optionally with UrQMD as an afterburner) to investigate the hadronic resonance production and interaction in Pb+Pb collisions at $\sqrt{s_{NN}} = 2.76$ TeV and compared their results to data from the ALICE Collaboration. Their calculations reproduce the data very well for the different centralities. The simulation also showed that a large part of the resonances at low p_T cannot be reconstructed due to the final state interactions of their decay daughters.

Our goal is to investigate the dynamics of K^* vector-meson resonances using the Parton-Hadron-String Dynamics transport approach [2] employing the in-medium effects of the K^* s from the self-consistent coupled-channel unitary G-Matrix approach for the production of K^* s from the hadronic channels as well as from a QGP by microscopic dynamical hadronization. The in-medium effects have been already successfully used to model the

off-shell behaviour of the kaons K and antikaons \bar{K} at finite nuclear baryon density in Refs. [23–28]. Previously, we have evaluated within this framework the properties of the strange vector resonances as a function of the nuclear baryon density [29] and now incorporate the off-shell behaviour of the K^* s in form of a relativistic Breit-Wigner spectral function into PHSD. We recall that the PHSD transport approach incorporates the hadronic and partonic degrees-of-freedom and their interactions, dynamical hadronization and further off-shell dynamics in the hadronic stage which allows to include in a consistent way in-medium effects for hadrons as well as partons.

Throughout this paper we will follow the following convention: when addressing strange vector mesons consisting of an anti-strange quark, i.e. $K^{*+} = (u\bar{s})$ and $K^{*0} = (d\bar{s})$ we will refer them as $K^* = (K^{*+}, K^{*0})$; while for mesons with a strange quark, i.e. $K^{*-} = (\bar{u}s)$ and $\bar{K}^{*0} = (\bar{d}s)$ we will use notation as $\bar{K}^* = (K^{*-}, \bar{K}^{*0})$.

This paper is organized as follows: In section II we shortly recall the PHSD transport approach and its implementations beyond the cascade level. In section III we discuss the K^* vector-meson resonance in-medium effects; the first part describes the calculation of the in-medium effects using the G-matrix model while the second part contains the implementation of these effects into the PHSD. In section IV we then investigate the properties and the dynamics of the K^* vector-meson resonances in the PHSD for Au+Au collisions at the top RHIC energy, analyze the different production channels, the actual baryon densities explored as well as the in-medium effects of the K^* spectral functions. In section V we present our results in comparison to experimental data; the first part shows a comparison for p+p collisions while the second part contains a detailed confrontation with experimental data from the STAR Collaboration for A+A collisions including in particular the effect of acceptance cuts. Finally, we give a summary of our findings in section VI.

II. REMINDER OF PHSD

The Parton-Hadron-String Dynamics (PHSD) is a non-equilibrium microscopic transport approach [30, 31] that incorporates hadronic as well as partonic degrees-of-freedom. It solves generalised (off-shell) transport equations on the basis of the off-shell Kadanoff-Baym equations [32–34] in first-order gradient expansion. Furthermore, a covariant dynamical transition between the partonic and hadronic degrees-of-freedom is employed that increases the entropy in consistency with the second law of thermodynamics. The hadronic part is equivalent to the HSD transport approach [35, 36] which includes the baryon octet and decouplet, the 0^- and 1^- meson nonets and higher resonances. When the mass of the hadrons exceeds a certain value (1.5 GeV for baryons and 1.3 GeV for mesons) the hadrons are treated as strings (or continuum excitations) that decay to hadrons within a for-

mation time of ~ 0.8 fm/c using the LUND string decay [37]. In PHSD the partonic, or the QGP phase, is based on the Dynamical Quasi-Particle Model (DQPM) [34, 38] which describes the properties of QCD (in equilibrium) in terms of resummed single-particle Green's functions. Instead of massless partons the gluons and quarks in PHSD are massive strongly-interacting quasi-particles whose masses are distributed according to spectral functions (imaginary parts of the complex propagators). The widths and pole positions of the spectral functions are defined by the real and imaginary parts of the parton self-energies and the effective coupling strength in the DQPM is fixed by fitting respective lQCD results from Refs. [39, 40] (using in total three parameters).

In the beginning of the nucleus-nucleus collision the LUND string model [41] is used to create colour neutral strings from the initial hard nucleon scatterings, i.e. the formation of two strings takes place through primary NN collisions. These early strings dissolve into massive coloured quarks and anti-quarks in their self-generated mean-field as described by the DQPM [42] if the energy density is above the critical energy density $\mathcal{E} = 0.5 \text{ GeV}/\text{fm}^{-3}$ in line with lQCD [43]. If the energy density is below critical the strings decay to pre-hadrons (as in case of p+p reactions or in the hadronic corona). The QGP phase is then evolved by the off-shell transport equations with self-energies and cross sections from the DQPM. When the fireball expands the probability of the partons for hadronization increases close to the phase boundary (crossover at all RHIC energies), the hadronisation takes place using covariant transition rates and the resulting hadronic system is further on governed by the off-shell HSD dynamics incorporating (optionally) self-energies for the hadronic degrees-of-freedom [19].

Thus in the PHSD approach the full evolution of a relativistic heavy-ion collision, from the initial hard NN collisions out of equilibrium up to the hadronisation and final interactions of the resulting hadronic particles, is described on the same footing. We recall that this approach has been successfully employed for p+p, p+A and A+A reactions from about $\sqrt{s_{NN}} = 8 \text{ GeV}$ to 2.76 TeV (see the review [2]).

In this study we will concentrate on the strange resonance dynamics mainly at RHIC energies where the PHSD describes well the bulk observables, i.e. rapidity, p_T -spectra, v_n coefficients etc. [2].

III. K^* IN MEDIUM

Before coming to actual results from PHSD for p+p and A+A collisions at relativistic energies we describe in some detail the evaluation of the kaon, antikaon and K^* selfenergies as a function of baryon density and their implementation in the PHSD. The medium properties and the off-shell propagation of the strange vector-meson resonances K^* and \bar{K}^* are based on the “G-Matrix” approach from Refs. [29, 44]. We use this approach to

calculate the self-energy of the K^* and \bar{K}^* which we then implement in the form of relativistic Breit-Wigner spectral functions into PHSD to model the in-medium effects and off-shell propagation of the K^* and \bar{K}^* within a transport approach.

A. G-Matrix approach

In recent years some efforts have been undertaken to assess the interaction of vector mesons with baryons in coupled-channel effective field approaches. In Refs. [11–13] vector mesons are introduced within the Hidden Local Symmetry approach [14–17] and a tree-level vector-meson baryon s -wave scattering amplitude is derived as the low-energy limit of a vector-meson exchange mechanism. In Ref. [45] the interaction of vector mesons with baryons is obtained on the basis of a $SU(6)$ spin-flavor symmetry extension of standard $SU(3)$ meson-baryon chiral perturbation theory, leading to a generalized (s -wave) Weinberg-Tomozawa interaction between the pseudoscalar/vector meson octets and the octet and decuplet of baryons. These two models share a crucial feature, namely, several N^* and hyperon resonances are dynamically generated in a broad range of energies upon unitarization of the leading order (LO), tree-level amplitudes. Such states are indicative of non-trivial meson-baryon dynamics and one may expect an impact on the in-medium properties of strange vector mesons. Incidentally, the properties of vector mesons within these approaches were initially investigated for the case of the $\bar{K}^*(892)$ [44]. The self-energy of the ω meson was also updated recently along the same ideas in [46].

The absence of baryonic resonances with $S = +1$ close to threshold induces milder nuclear medium effects in the properties of the K meson [24, 28] as compared to the \bar{K} meson, whose behaviour is largely dominated by the $\Lambda(1405)$ resonance appearing in s -wave $\bar{K}N$ scattering. A similar situation takes place for the vector partner of the K , the K^* meson. Note that the K^* decays predominantly into $K\pi$, and therefore not only collisional effects but its in-medium decay width has to be taken into account (we come back to this point below). However, since the K meson itself is barely influenced by nuclear matter one can anticipate small changes in $\Gamma_{K^*, \text{dec}}$ as compared to the vacuum case.

An effective Lagrangian approach, as developed in [12], was used in our previous study [29] to calculate the K^* meson self-energy at threshold energy. In this approach, the interaction between the octet of light vector mesons and the octet of $J^P = 1/2^+$ baryons is built within the hidden local gauge symmetry (HLS) formalism, which allows to incorporate vector meson interactions with pseudoscalar mesons respecting the chiral dynamics of the pseudoscalar meson-meson sector. The interactions of vector mesons with baryons are assumed to be dominated by vector-meson exchange diagrams, which incidentally allows for an interpretation of chiral Lagrangians

in the meson-baryon sector as the low-energy limit of vector-exchange mechanisms naturally occurring in the theory. Vector-meson baryon amplitudes emerge in this scheme at leading order, in complete analogy to the pseudoscalar-meson baryon case, via the self-interactions of vector-meson fields in the HLS approach. At small momentum transfer (i.e., neglecting corrections of order p/M , with M the baryon mass), the LO s -wave scattering amplitudes have the same analytical structure as the ones in the pseudoscalar-meson baryon sector (Weinberg-Tomozawa interaction), namely

$$\begin{aligned} V_{ij} &= -C_{ij} \frac{1}{4f^2} (2\sqrt{s} - M_{B_i} - M_{B_j}) \times \\ &\quad \times \left(\frac{M_{B_i} + E_i}{2M_{B_i}} \right)^{1/2} \left(\frac{M_{B_j} + E_j}{2M_{B_j}} \right)^{1/2} \vec{\varepsilon} \cdot \vec{\varepsilon}' \\ &\simeq -C_{ij} \frac{1}{4f^2} (q^0 + q'^0) \vec{\varepsilon} \cdot \vec{\varepsilon}', \end{aligned} \quad (1)$$

where q^0 (q'^0) stands for the energy of the incoming (outgoing) vector meson with polarisation $\vec{\varepsilon}$ ($\vec{\varepsilon}'$), C_{ij} stand for channel-dependent symmetry coefficients [12], and the latin indices label a specific vector-meson baryon (VB) channel, e.g., $K^{*+}p$.

The K^* collisional self-energy follows from summing the forward K^*N scattering amplitude over the allowed nucleon states in the medium, schematically $\Pi_{K^*}^{\text{coll}} = \sum_{\vec{p}} n(\vec{p}) T_{K^*N}$. Due to the absence of resonant states nearby, a $t\rho$ approximation is well justified at energies sufficiently close to threshold, which leads to the practical result (take $T = V$ here)

$$\begin{aligned} \Pi_{K^*}^{\text{coll}} &= \frac{1}{2} (V_{K^{*+}p} + V_{K^{*+}n}) \rho_0 \left(\frac{\rho}{\rho_0} \right) \\ &\simeq \alpha \frac{M_K}{M_{K^*}} M_{K^*}^2 \left(\frac{\rho}{\rho_0} \right), \end{aligned} \quad (2)$$

with $\alpha = 0.22$, leading to a positive mass shift (equivalent to a repulsive optical potential) of about $\delta M_{K^*} \simeq 50$ MeV at normal matter density $\rho = \rho_0 = 0.17 \text{ fm}^{-3}$ (recall $\delta M_{K^*} \simeq \text{Re} \Pi_{K^*} / 2M_{K^*}$). Replacing the lowest order tree level amplitudes V in the former result by unitarized amplitudes in coupled channels (solving the Bethe-Salpeter equation, $T = V + VGT$) one finds a reduction by roughly one third over the previous result, namely $\delta M_{K^*}(\rho_0) \simeq 30$ MeV [i.e. $\alpha \simeq 0.13$ in Eq. (2)]. Further medium corrections on the vacuum scattering amplitudes T_{K^*N} , leading to a full G -matrix calculation, are of marginal relevance in the present case due to the mild corrections introduced by the smoothly energy-dependent K^*N interaction¹.

In the case of the \bar{K}^* , the collisional part of the self-energy, related to the quasi-elastic reaction $\bar{K}^*N \rightarrow \bar{K}^*N$ and accounting for absorption channels, induces a strong broadening of the \bar{K}^* spectral function as a result of the mixing with two $J^P = 1/2^-$ states, the $\Lambda(1783)$ and $\Sigma(1830)$, which are dynamically generated in the hidden local symmetry approach in a parallel way to the $\bar{K}N$ interaction and the $\Lambda(1405)$. Such complicated many-body structure of the \bar{K}^*N interaction requires a detailed analysis of medium corrections such as Pauli blocking on baryons and a self-consistent evaluation of the in-medium \bar{K}^*N scattering amplitude (G -matrix) and the \bar{K}^* self-energy, as was done in [44]. For the present study we recourse to a suitable parameterization of the resulting \bar{K}^* self-energy and spectral function, which we discuss in more detail below.

As mentioned before, the decay with of the K^*/\bar{K}^* meson (with suitable medium corrections) has to be taken into account to realistically assess production and annihilation rates. Such effects are readily incorporated for the \bar{K}^* within the G -matrix approach which we parametrize from Ref. [44]. For the K^* , instead, we evaluate explicitly its medium-modified $K^* \rightarrow K\pi$ width as follows [29],

$$\Gamma_{V,\text{dec}}(\mu, \rho) = \Gamma_V^0 \left(\frac{\mu_0}{\mu} \right)^2 \frac{\int_0^{\mu - m_\pi} q^3(\mu, M) A_j(M, \rho) dM}{\int_{M_{\min}}^{\mu_0 - m_\pi} q^3(\mu_0, M) A_j(M, 0) dM}, \quad (3)$$

where $j = K$ and $V = K^*$ for the present case, $q(\mu, M) = \sqrt{\lambda(\mu, M, M_\pi)} / 2\mu$ and $\lambda(x, y, z) = [x^2 - (y + z)^2][x^2 - (y - z)^2]$. Γ_V^0 stands for the vector meson (vacuum) partial decay width in the considered channel and μ_0 is the nominal resonance mass, particularly $\Gamma_{K^*, \bar{K}^*}^0 = 42$ MeV and $\mu_0 = 892$ MeV [48]. Eq. (3) accounts for the in-medium modification of the resonance width by its decay products. In particular, we consider the fact that kaons and anti-kaons may acquire a broad spectral function in the medium, $A_j(M, \rho)$. As discussed in [29], A_K in Eq. (3) is a delta function in vacuum since the kaon is stable in vacuum with respect to the strong interaction, and to a good approximation the same can be kept at finite nuclear density by using an effective kaon mass $M_K^{*2}(\rho) = M_K^2 + \Pi_K(\rho)$ with $\Pi_K(\rho) \simeq 0.13 M_K^2(\rho/\rho_0)$ [28, 49, 50]. In general this may not be the case for other vector mesons even in the vacuum case, e.g., $a_1 \rightarrow \rho\pi$, where the ρ meson has a large width into two pions (M_{\min} then stands for the corresponding threshold energy).

Once both collisional and decay self-energies are obtained, the K^* and \bar{K}^* spectral function is readily given as the imaginary part of the vector-meson in-medium propagator, namely,

$$\begin{aligned} S_V(\omega, \vec{q}; \rho) &= -\frac{1}{\pi} \text{Im} D_V(\omega, \vec{q}; \rho) \\ &= -\frac{1}{\pi} \frac{\text{Im} \Pi_V(\omega, \vec{q}; \rho)}{[\omega^2 - \vec{q}^2 - M_V^2 - \text{Re} \Pi_V(\omega, \vec{q}; \rho)]^2 + [\text{Im} \Pi_V(\omega, \vec{q}; \rho)]^2}. \end{aligned} \quad (4)$$

¹ To be precise, we use the term G -matrix for the in-medium effective meson-baryon T -matrix obtained in DiracBrueckner theory. [47]

with $V = K^*, \bar{K}^*$, where Π_V contains the sum of the collisional and decay self-energies.

B. Implementation in PHSD

In order to implement K^* and \bar{K}^* in-medium properties in PHSD we adopt a relativistic Breit-Wigner prescription for the strange vector meson spectral functions ($V = K^*, \bar{K}^*$) [29, 51],

$$A_V(M, \rho) = C_1 \frac{2}{\pi} \frac{M^2 \Gamma_V^*(M, \rho)}{(M^2 - M_V^{*2}(\rho))^2 + (M \Gamma_V^*(M, \rho))^2}, \quad (5)$$

where M is the invariant mass and C_1 is a normalisation constant ensuring that the sum rule

$$\int_0^\infty A_V(M, \rho) dM = 1 \quad (6)$$

is fulfilled. The connection with the spectral function in Eq. (4) can be done by setting the vector-meson momentum at zero,

$$A_V(M, \rho) = 2 \cdot C_1 \cdot M \cdot S_V(M, \vec{0}, \rho), \quad (7)$$

a practical approximation which does not account for explicit energy and momentum dependence of medium corrections (this limitation is consistently dealt with by considering vector mesons to be at rest in the nuclear matter frame when evaluating their self-energy). The in-medium mass M_V^* and decay width Γ_V^* of the K^*/\bar{K}^* are derived from the vector meson self-energy, as in the case of partons in the DQPM,

$$\begin{aligned} (M_V^*)^2 &= M_V^2 + \text{Re } \Pi_V(M_V^*, \rho), \\ \Gamma_V^*(M, \rho) &= -\text{Im } \Pi_V(M, \rho)/M, \end{aligned} \quad (8)$$

where M_V denotes the nominal (pole) mass of the resonance in vacuum.

We briefly comment in the following the essential features of the K^* and \bar{K}^* Breit-Wigner spectral functions when including medium effects along the self-energy calculation in the previous section. In Fig. 1 we depict the spectral function for the K^* meson. The K^* experiences a net repulsive interaction with the medium which leads to a shift of the spectral function's peak to higher invariant masses with increasing nuclear density. Overall, the width of the K^* becomes slightly smaller with increasing density, due to the kaon becoming also heavier (this effect is largely compensated by the higher K^* excitation energy). Furthermore, the threshold energy for the creation of a K^* is shifted up, i.e. $M_{th} = M_K + M_\pi + \Delta M(\rho) \approx 0.633 \text{ GeV} + \Delta M(\rho)$, with $\Delta M(\rho) \simeq \Pi_K(\rho)/2M_K$, which amounts to $0.06 M_K$ at normal matter density.

Interestingly, in case of the vector antikaon \bar{K}^* the effects from the medium are rather different as compared to the K^* . Fig. 2 shows the spectral function for the \bar{K}^*

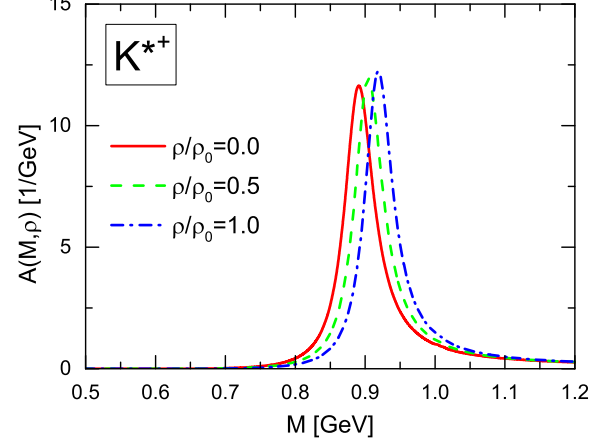


FIG. 1: The relativistic Breit-Wigner spectral function $A(M, \rho)$ of the K^* is shown as a function of the invariant mass M for different nuclear densities. The solid red line corresponds to the vacuum spectral function, whereas the dashed green and the dash-dotted blue lines correspond to densities $\rho/\rho_0 = 0.5, 1.0$, respectively.

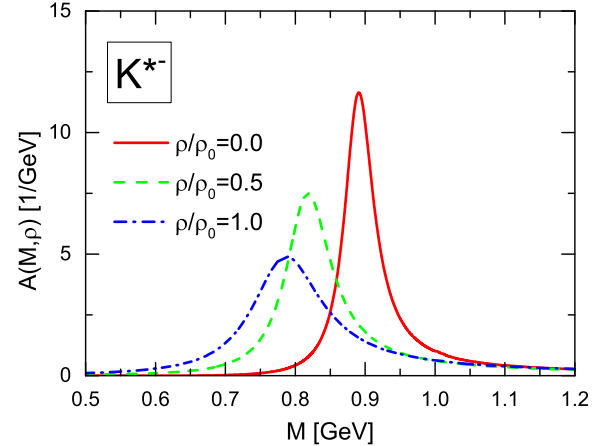


FIG. 2: Same as Fig. 1 for the \bar{K}^* spectral function.

at different nuclear densities. The distribution is considerably shifted to lower invariant masses when the density is increased, reflecting the overall attractive interaction of the \bar{K}^* with the baryon-rich medium. Furthermore, the \bar{K}^* width is largely enhanced as a consequence of the multiple absorption channels that are accounted for in the \bar{K}^* self-energy, involving the mixing of the quasi-particle mode with ΛN^{-1} and ΣN^{-1} excitations. Consequently, the threshold energy for the creation of a \bar{K}^* is considerably diminished, almost down to $M_{th} \sim 2M_\pi$, which implies that an off-shell \bar{K}^* can be created at rather low invariant masses.

The medium corrections discussed before have an

impact on the K^* and \bar{K}^* production rates in the hadronic phase of a heavy-ion collision. The production/annihilation cross section in PHSD is consistently modified according to

$$\sigma_{K^*(\bar{K}^*)}(M, \rho) = \frac{6\pi^2 A_{K^*(\bar{K}^*)}(M, \rho) \Gamma_{K^*(\bar{K}^*)}^*(M, \rho)}{q(M, M_K, M_\pi)^2}. \quad (9)$$

Fig. 3 shows the cross-section for K^* production from $\bar{K}\pi$ scattering. The evolution of the cross section with the nuclear density reflects that of the K^* spectral function, leading to a shift of the energy distribution to higher invariant masses. The presence of the Γ^* factor in Eq. 9, accounting for the effective $\bar{K}^*\bar{K}\pi$ coupling and multiplying the spectral function, makes the maximum value of the cross section practically unchanged when varying the density, reaching a value as large as 160-170 mb. The observed shift of the cross-section implies that, in order to create K^* at finite densities, larger energies are needed as compared to the same reaction in vacuum.

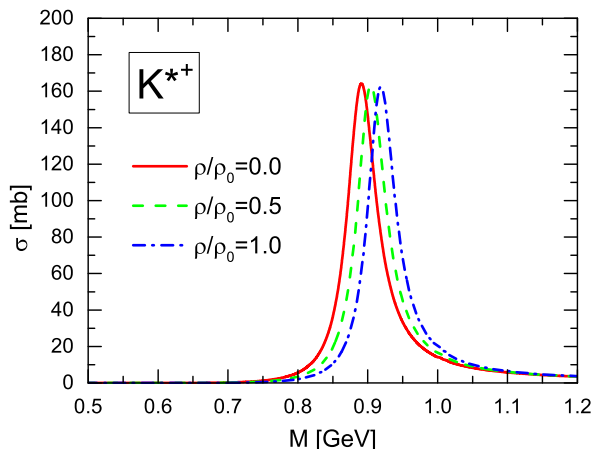


FIG. 3: The cross-section σ for K^* production/annihilation is shown as a function of the invariant mass M for different nuclear densities. The solid red line corresponds to the vacuum case, whereas the dashed green and the dash-dotted blue lines correspond to densities $\rho/\rho_0 = 0.5, 1.0$, respectively.

Quite different is the behavior of the \bar{K}^* cross section, as can be seen in Fig. 4. The energy dependence reflects the attractive nature of the \bar{K}^* interaction with the nuclear medium, as follows from the \bar{K}^* spectral function, the peak of the distribution being shifted to lower invariant masses in the same magnitude as the density is increased. The fall in the maximum of the cross section, though, seems to saturate due to the large increase of the \bar{K}^* width. At nuclear matter density, the cross section reaches a maximum value around 100 mb at invariant masses around 120 MeV below the vacuum case.

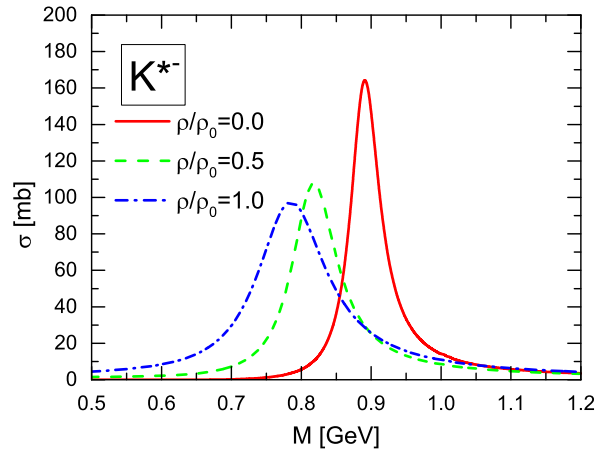


FIG. 4: Same as in Fig. 3 for the \bar{K}^* production/annihilation cross section.

IV. K^* DYNAMICS IN PHSD

Before we come to the physical observables that can be compared to experimental data we investigate the on/off-shell dynamics of the K^* vector mesons within the PHSD transport approach for central Au+Au collisions at $\sqrt{s_{NN}} = 200$ GeV. We will investigate the main production channels of the K^* mesons, their production in time and record the baryon density at production. In order to better understand the experimental results in the next section we also investigate the change of the transverse momentum spectrum with respect to the experimental cuts imposed for the reconstruction the K^* vector mesons.

A. Production channels and dependence on baryon density

We start with the production of the strange vector mesons as a function of time for the different production channels in PHSD.

As can be seen from Fig. 5 there is no sizeable difference between the number of vector kaons K^* and vector antikaons \bar{K}^* s from PHSD. The production by strings in the hadronic corona occurs early and gives practically no further contribution in the late stages. Furthermore, one can see that the contribution from the QGP is not very large and starts a few fm/c later in the hadronization, when compared to the late $K + \pi$ channel (blue lines). In fact, the QGP contribution is on the same level as the contribution from strings for this system. For times larger than 150 fm/c (not shown here) also the $K + \pi$ channel decreases rapidly and all vector mesons simply decay.

With respect to in-medium modifications of the vector mesons the baryon density at the production point is of

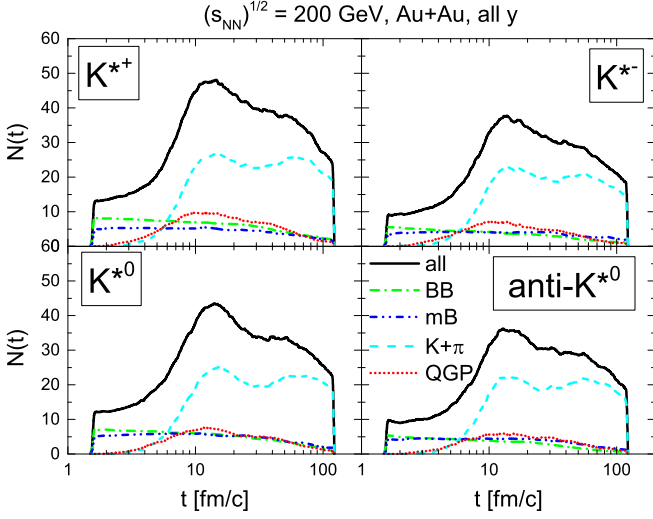


FIG. 5: The number of strange vector mesons $N(t)$ is shown as a function of time t for all four isospin channels of the K^* mesons and for all production channels in central Au+Au collisions at $\sqrt{s_{NN}} = 200$ GeV (all y) from a PHSD calculation. The upper left panel shows the channel decomposition for the K^{*+} , the upper right panel shows the channel decomposition for the K^{*-} , the lower left panel shows the channel decomposition of the K^{*0} and the lower right panel shows the channel decomposition of the \bar{K}^{*0} . The legend for all four panels is as follows: the solid black line shows all produced K^* s, the dash dotted green line shows K^* s produced from baryon-baryon strings, the solid dash double-dotted line shows K^* s produced from meson-baryon strings, the dashed light blue line shows K^* s produced from $K + \pi$ annihilation and the short dotted red line shows K^* produced during the hadronisation of the QGP.

additional interest. Fig. 6 shows the normalised number of K^* s for two collision energies as a function of the baryon density $\frac{\rho}{\rho_0}$ for central Au+Au collisions. From the previous figures we know that most of the K^* s come from the $K + \pi$ channels in the later stage. Accordingly, most of the K^* s are created while the baryon density is fairly low, with only very few mesons created above half normal nuclear baryon density ρ_0 during a Au+Au collision with a cms energy of 200 GeV at RHIC. Thus the in-medium modifications of the strange vector mesons are expected to be small at this energy as well as observable consequences in the final spectra. Note, however, that for a much lower collisional energy of 10 GeV the baryon densities are much higher and the perspectives to see in-medium modifications of the vector mesons become better. The situation is not very different from the dilepton measurements in heavy-ion reactions with respect to the contribution from the ρ -meson decay [2].

Furthermore, one can see in Fig. 7 the channel decomposition of the K^* as a function of the baryon density (in units of ρ_0). As before the dominant channel is the $K + \pi$ channel. It is important to note that this is the case for

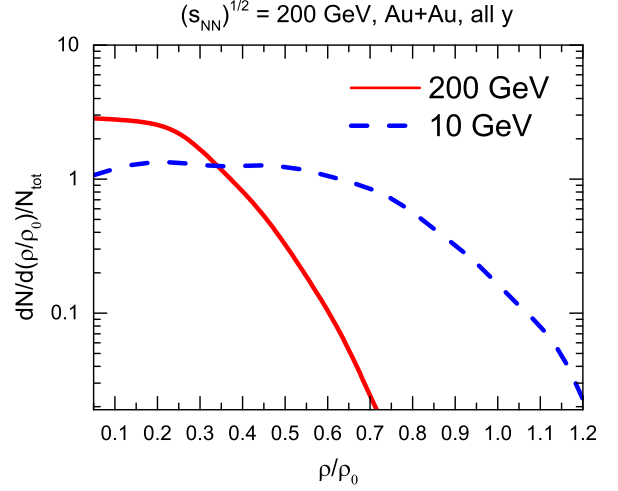


FIG. 6: The differential distribution of the total number of K^* s $\frac{1}{N_{tot}} \frac{dN}{d(\frac{\rho}{\rho_0})}$ versus baryon density $\frac{\rho}{\rho_0}$ for Au+Au collisions at different cms energies from the PHSD simulations. The solid red line shows results for a collision at $\sqrt{s_{NN}} = 200$ GeV while the dashed blue line shows results for a collision at $\sqrt{s_{NN}} = 10$ GeV.

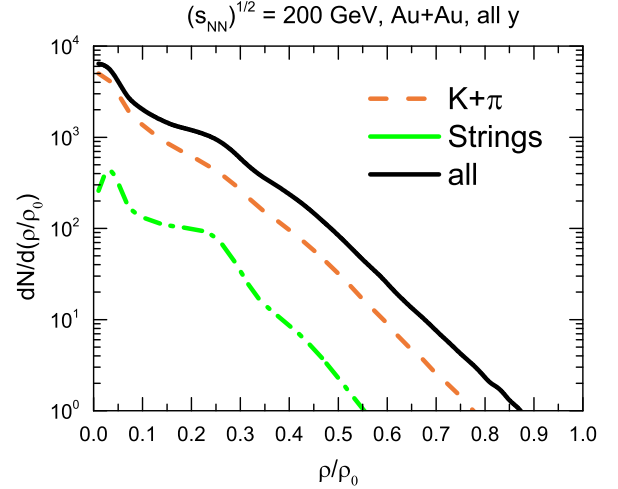


FIG. 7: The differential distribution $\frac{dN}{d(\frac{\rho}{\rho_0})}$ as a function of the baryon density $\frac{\rho}{\rho_0}$ for Au+Au collisions at a cms energy of $\sqrt{s_{NN}} = 200$ GeV for different production channels of the K^* . The solid black line shows the K^* s coming from all production channels, the dashed orange line shows K^* s coming from the $K + \pi$ channel and the dash dotted green line shows K^* s coming from meson-baryon and baryon-baryon strings.

all baryon densities, since, as opposed to the other channels, K^* s coming from the $K + \pi$ channel are created throughout the whole collision history and can thus occur at low and higher baryon densities, respectively.

B. Modifications of the K^* mass distributions in the medium

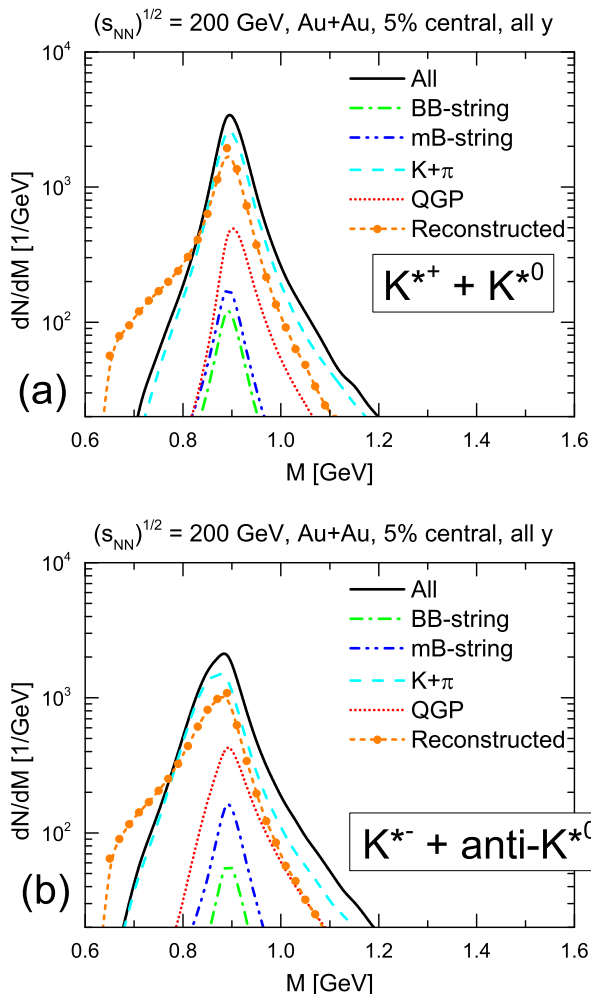


FIG. 8: The differential mass distribution $\frac{dN}{dM}$ for the vector kaons K^* ("a", upper part) and antikaons \bar{K}^* ("b", lower part) for different production channels as a function of the invariant mass M in a Au+Au collision at $\sqrt{s_{NN}} = 200$ GeV from a PHSD calculation. The solid black lines show all produced K^* (\bar{K}^*)s, the dash dotted green lines indicate production from baryon-baryon strings, the dash double-dotted blue lines – from meson-baryon strings, the dashed light blue lines – from $K + \pi$ ($\bar{K} + \pi$) annihilation and the short dotted red line correspond to the production during the hadronisation of the QGP. The dashed orange line with the circles shows the distribution for K^* s that have been reconstructed from final kaon and pion pairs.

As can be seen in Fig. 8 again the dominant production channel of the vector kaons K^* ("a", upper part) and vector antikaons \bar{K}^* ("b", lower part) is the annihilation of the $K + \pi$ ($\bar{K} + \pi$) pairs. Due to its broad structure the spectral function of the K^* and \bar{K}^* allows for the annihilation of $K + \pi$ pairs also at lower and higher masses as compared to the vacuum. The contribution from meson-

baryon and baryon-baryon strings is practically negligible, however, there is still a sizeable contribution coming from the QGP. The shape of the spectral function for vector kaons suggests that there should be some K^* s produced at higher invariant masses due to finite baryon densities where the pole mass is shifted up. However, the high baryon density region is not much populated at this cms energy as demonstrated above such that these effects will be hard to disentangle in the final spectra in comparison to experiment.

As seen from the lower part ("b") of Fig. 8 the mass distribution of the vector antikaons is slightly shifted to the low masses which stems from the shift of the spectral function of the \bar{K}^* to lower masses at finite baryon densities. This means that in-medium effects are still present since the mesons are created at nonzero densities. The contribution of the strings and the QGP does not play a significant role due to the lack of baryons relative to mesons at the top RHIC energy.

In both of these figures the distribution for the reconstructed particles is shifted from higher to lower invariant mass regions. Furthermore the total number of particles is reduced to about 40 to 50 % in the reconstructed distribution as opposed to the particles that were taken from the decay point.

We point out that in the present study we discard the medium modification of the K^* spectral function due to "thermal" effects, i.e. due to the interaction with mesons. According to our previous study [29] this leads to minor changes of the K^* spectral function at finite temperatures up to $T_C = 158$ MeV where the crossover transition to the QGP occurs in the PHSD. We note that according to the study by Cho and Lee [52] such thermal effects become visible in the interaction rates of K^* s essentially at higher temperatures.

C. Transverse momentum distributions and acceptance cuts

Before we compare our PHSD results with experimental data, we have to establish the restrictions that arise during the reconstruction of the K^* mesons from final $K + \pi$ pairs on the observables. In Fig. 9 we show PHSD results for K^{*0} and \bar{K}^{*0} at midrapidity for central Au+Au collisions at the top RHIC energy. We recall that in PHSD we can study the K^* s at their decay point, i.e. at the point in space-time of their decay into $K + \pi$ pairs. Furthermore, we can reconstruct the K^* s from their daughter particles, the K and π pairs that are affected by final state interactions. In Fig. 9 one can see that there is a slight difference between the decayed K^* s, shown by the dashed black line, and the reconstructed K^* s, shown by the red line. This difference is due to rescattering and absorption of the final kaons and pions in the medium. Particles with low transverse momentum are more affected by this than particles with higher transverse momentum, and these two lines merge

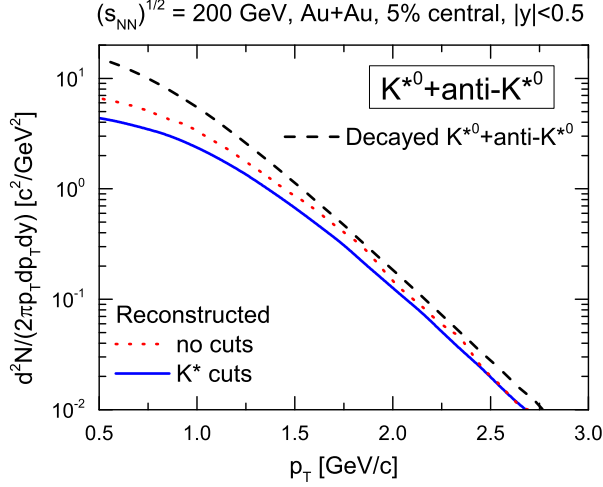


FIG. 9: The transverse momentum spectrum $d^2N/(2\pi p_T dp_T dy)$ versus the transverse momentum p_T for vector kaons and antikaons in Au+Au collisions at $\sqrt{s_{NN}} = 200$ GeV from the PHSD simulation. The dashed black line shows the spectrum directly at the point when the \bar{K}^* decays in the PHSD simulation. The dotted red and solid blue lines show the spectrum after the \bar{K}^* has been reconstructed from the final kaons and pions. The dotted red line does not include any cuts while the solid blue line includes cuts on the invariant mass of the \bar{K}^* .

with increasing p_T . This implies that fast K^* s can be reconstructed much more efficiently since their daughter particles do not interact with the medium as much as particles with lower p_T which rescatter more often due to their low velocities in the hadronic medium.

Fig. 9 also shows the K^* s that have been reconstructed from final particles (blue line) employing the restrictions that have been imposed on the K^* in the form of a restriction to a specific invariant mass region of $M = [0.8, 1.0]$ GeV. This is due to the low signal to noise ratio during the reconstruction of the K^* . While the spectral function of the K^* is relatively broad, with a width of about 42 MeV in vacuum, the experimental signal is very narrow and it is difficult to distinguish correlated from uncorrelated $K + \pi$ pairs below and above the selected invariant mass region.

It is also important to note the different production channels of the K^* in actual observables, e.g. the transverse momentum spectrum where different channels might reflect different spectral slopes. This is shown in Figs. 10 for vector kaons K^* (upper part) and vector antikaons \bar{K}^* (lower part), respectively. Similarly to the figures in Fig. 8 one can see that K^* s coming from meson-baryon and baryon-baryon strings contribute only a small part to the overall spectrum. The far dominant channel contribution comes from $K + \pi$ annihilation in the final hadronic stage. The second-largest contribution comes from the QGP, however, it is smaller by about an order of magnitude for all p_T which makes the K^* less suitable as a probe for the QGP. Furthermore, the spec-

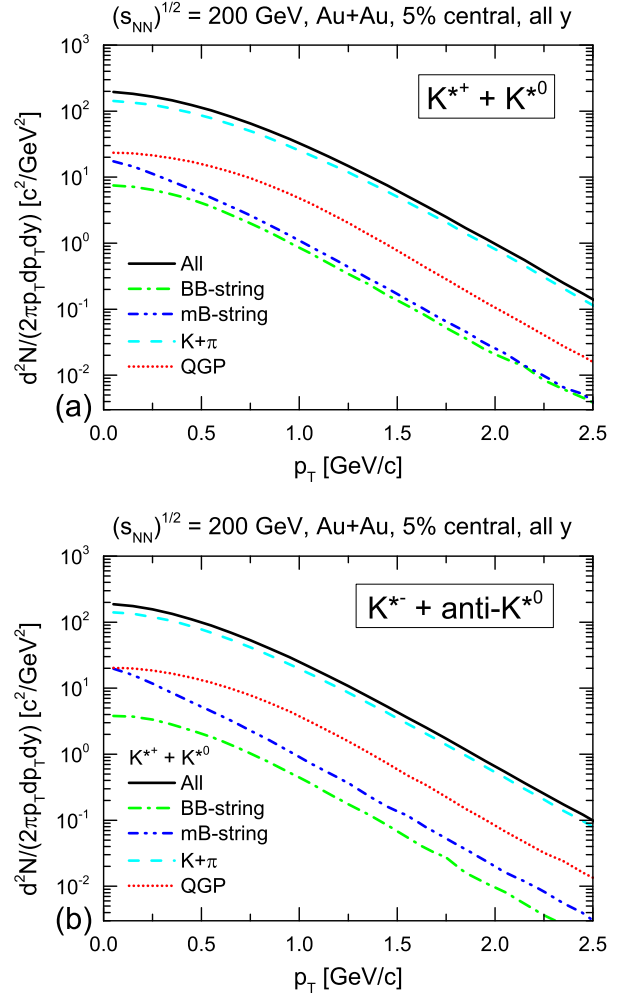


FIG. 10: The channel decomposition of the transverse momentum spectrum $d^2N/2\pi p_T dp_T dy$ for K^* (upper part) and for the \bar{K}^* (lower part) for different productions channels in Au+Au collisions at a cms energy of $\sqrt{s_{NN}} = 200$ GeV from a PHSD calculation: the solid black lines show all produced K^* (\bar{K}^*)s, the dash dotted green lines indicate production from baryon-baryon strings, the dash double-dotted blue lines – from meson-baryon strings, the dashed light blue lines – from $K + \pi$ ($\bar{K} + \pi$) annihilation and the short dotted red lines correspond to the production during the hadronisation of the QGP.

tral slopes from all channels are very similar in the high p_T region. This is true for both K^* s and \bar{K}^* s.

D. Production and decay time of the K^*

In order to understand better which K^* s can be seen or reconstructed in the detector at an experiment like STAR one can look at when the K^* s are produced and when they decay during a heavy-ion collision. As can be seen in fig. 5 different channels dominate the K^* production during certain times of a heavy-ion collision. Thus one

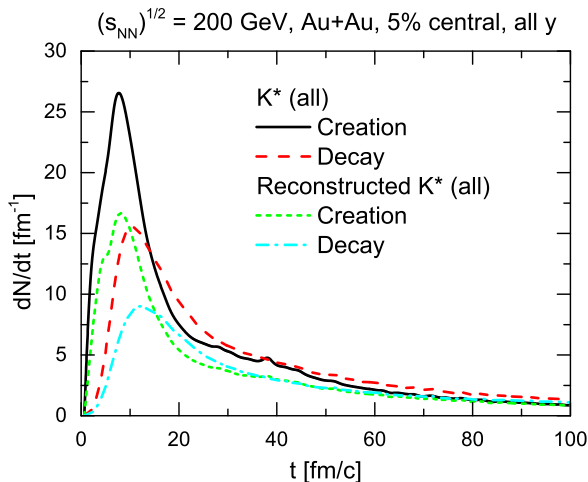


FIG. 11: The creation and decay rates versus time for central Au+Au collision at a cms energy of $\sqrt{s_{NN}} = 200$ GeV. Both the K^* s and \bar{K}^* s are included. The solid black and dashed red lines show the creation and decay rates for all K^* s in a system. The short-dashed green and dash-dotted blue lines show the creation and decay rates respectively of K^* s that could be reconstructed from the final pions and kaons ($\pi + K$).

could deduce from what source the reconstructed $K\pi$ pair would originate.

Fig. 11 shows the production and the decay rates of all K^* s and \bar{K}^* which existed in a heavy-ion collisions (solid black and dashed red lines) and which of these K^* s could be reconstructed in the detector from the final pions and kaons ($\pi + K$) – short-dashed green and dash-dotted blue lines.

As can be seen many of the K^* s that decay during the early stages of the collision, up to a time of $t = 20$ fm/c, decay into $K\pi$ pairs that do not reach the detector and thus cannot be reconstructed due to absorption by the medium or rescattering of the final pions and kaons. During later stages of the collision, however, the K^* s that are created (most probably from $K\pi$ collisions, as can be seen in fig. 5) can also be seen in the detector, since the medium is already dilute and absorption of the decay particles by the medium is rare.

V. RESULTS FROM PHSD IN COMPARISON TO DATA FROM STAR

In this section we present our results from the PHSD transport approach in comparison to the data from the STAR Collaboration at RHIC. [7–10]

The STAR collaboration at RHIC has investigated the following hadronic decay channels: $K(892)^{*0} \rightarrow K^+\pi^-$, $K(892)^{*0} \rightarrow K^-\pi^+$ and $K(892)^{*0} \rightarrow K_S^0\pi^\pm \rightarrow \pi^+\pi^-\pi^\pm$ [7]. As has been mentioned above the K^* reconstruction relies on the final particles observed in the detector, i.e. the kaons and the pions. Since both decay products

suffer from rescattering and absorption the reconstruction becomes difficult. Furthermore, the time resolution and accuracy in momentum and invariant mass of the detector itself adds another hurdle to a reconstruction of the K^* signal due to a possible misidentification of the particles.

The procedure for obtaining the K^* signal is based on the combination of all kaons and pions with respect to the hadronic decay channels mentioned above, i.e. only channels that are physically possible are taken. To get rid of the background there are several techniques that can be employed: i) One can take all unphysical channels and combine the kaons and pions to get the background spectrum. Another method to get the background is ii) to flip the x and the y component of the momentum of either the kaons and pions and combine all physical channels. A third method iii) consists of pairing all kaons and pions from two different events. Unlike the first two methods this method ensures that there can be no possible correlation between the kaons and the pions and thus is most suited to construct the background spectrum [53] since it is not possible that kaons and pions from different events can be correlated.

For the reconstruction of the $K^{*\pm}$ vertex cuts also need to be taken into account due to the second decay vertex which stems from the decay of the K_S^0 to a $\pi^+\pi^-$ pair. However, in PHSD this is not accounted for because the $K^{*\pm}$ directly decay to a K instead of a K_S [7].

In principle, the experimental reconstruction procedure could exactly be repeated with the PHSD final particle spectra on an event-by-event basis. However, this would imply to generate a huge amount of events which is very costly due to limited computing power. On the other hand the transport approach offers information that is not available in the experiment. We can precisely identify in PHSD the kaons and pions that correspond to a certain K^* decay and we can reconstruct the final K^* spectrum much more efficiently and also with high precision.

These different methods will not lead to a sizeable differences for p+p collisions, since the number of created particles is relatively small and the risk of mismatching particles is comparably low. It is possible (and likely) that there is a difference in A+A collisions. Our studies, however, have not shown a significant difference as compared to the correlation method.

A. p+p collisions

First of all, the experimental reconstruction of the K^* in p+p collisions doesn't lead to a strong distortion of the K^* signal since p+p collisions produce only a low amount of particles and the rescattering and absorption of the final kaons and pions is practically vanishing compared to A+A collisions. Furthermore, there are no modifications of the kaons by a medium.

As can be seen from both figures in Fig. 12 the results

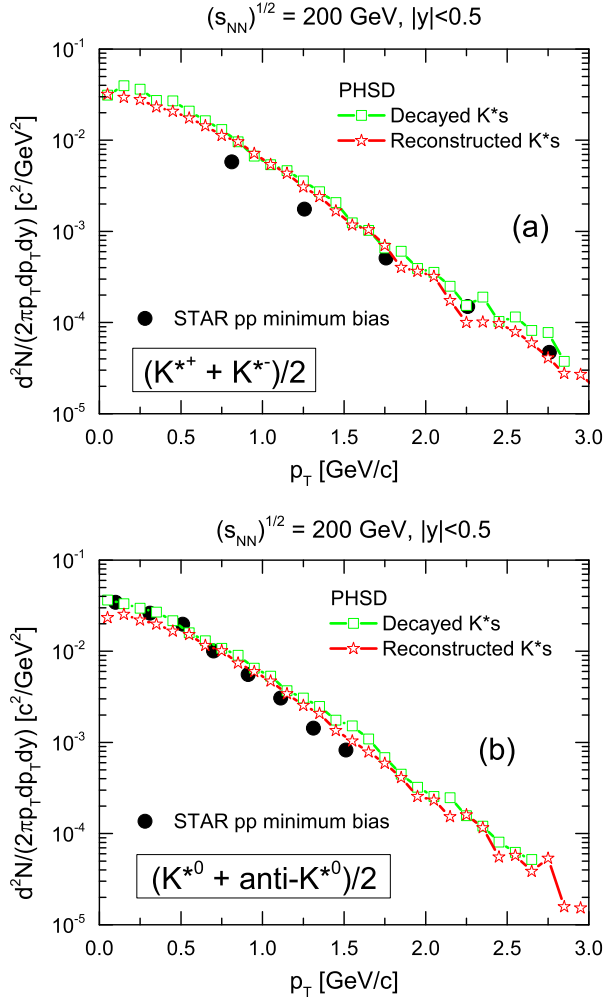


FIG. 12: The transverse momentum spectrum $d^2N/2\pi p_T dp_T dy$ versus the transverse momentum p_T for $K^{*+} + K^{*-}$ ("a", upper part) and $K^{*0} + \bar{K}^{*0}$ ("b", lower part) in a p+p collision at a cms energy of $\sqrt{s_{NN}} = 200$ GeV. The solid black circles denote minimum bias p+p data from the STAR experiment from Ref. [7]. The connected open symbols represent results from a PHSD simulation. The open green squares show results where the spectrum was obtained from the $K^*(\bar{K}^*)$'s coming directly from the decay point in PHSD. The open red stars show results from $K^*(\bar{K}^*)$'s that have been reconstructed from the final $K(\bar{K})$ and π pairs.

from the PHSD calculations reproduces the experimental data very well. The K^* spectrum from the reconstructed final kaons and pions matches the K^* spectrum from the K^* , which were directly taken from the decay point. This holds true for K^* s with both a zero and a non-zero electric charge. Experimentally all the possible K^* reconstruction channels are considered, through either a direct decay into a $K + \pi$ pair or indirectly through the second vertex calculation of the $K^0_S \rightarrow \pi^+ \pi^-$ decay. We note in passing that that PHSD appears to slightly underestimate the p_T slope for charged K^* s whereas it slightly overestimates the p_T slope for neutral K^* s. Since

in PHSD the slopes for charged and neutral K^* s are the same within statistical accuracy one might 'see' a slightly different slope in the STAR data. However, this is within the systematic uncertainties.

B. A+A collisions

The experimental reconstruction of the K^* spectrum in A+A collisions is a lot more complicated and the signal is much more more distorted. The number of produced particles in an Au+Au collisions is much higher than in a p+p collision which leads to a lot more background and to a higher probability of misidentification of particles. Furthermore, the cuts on the invariant mass have a large effect, as shown in IV.

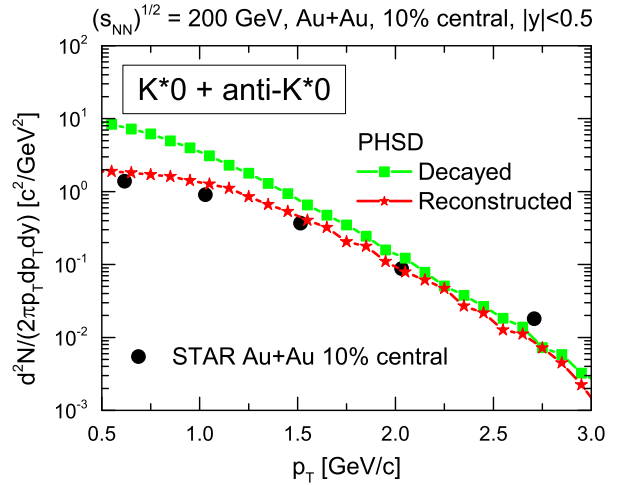


FIG. 13: The transverse momentum spectrum $d^2N/2\pi p_T dp_T dy$ versus the transverse momentum p_T for $K^{*0} + \bar{K}^{*0}$ mesons in a Au+Au collision at a cms energy of $\sqrt{s_{NN}} = 200$ GeV. The solid black circles show the data from the STAR Collaboration for 10% central collisions while the connected symbols show results from the PHSD calculation. The solid green squares show results where the K^* s were taken at the point of their decay while the solid red stars show results for K^* s that have been reconstructed from the final $K + \pi$ pairs. The STAR data are taken from Ref. [7].

Fig. 13 highlights the difference between the reconstructed K^* spectrum and the spectrum of K^* s taken directly from their decay point. While the reconstructed spectrum follows the experimental data very well after applying the acceptance cuts, the K^* spectrum as taken at the decay point is sizeably higher at low transverse momentum and has a lower slope. As has been discussed in the previous section only a small part of the change in the spectrum is due to rescattering and absorption by the medium. We have found that the dominant changes arise from the different cuts imposed in the reconstruction. This implies that parameters such as an effective

temperature T^* , which can be extracted from an exponential fit to the p_T spectra, do not necessarily correlate to the value that reflects the actual K^* decays during a collision. Both the cuts and the rescattering and absorption by the medium only affect the lower part of the transverse momentum spectrum while both the green and the red lines converge towards each other for higher p_T .

When considering rescattering and absorption effects one may argue that the faster kaons and pions, i.e. particles with a higher p_T , are able to escape the medium and reach the detector without sizeable interaction with the medium while particles with lower transverse momentum experience stronger final state interactions which lead to a distortion of the reconstructed K^* spectrum. Since the size of the 'fireball' changes with centrality the K^* spectra for different centrality classes provide further information.

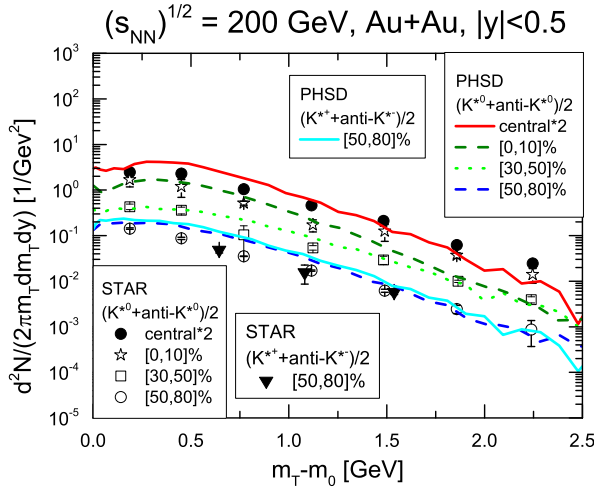


FIG. 14: The transverse mass spectrum $d^2N/2\pi m_T dm_T dy$ as a function of the transverse mass $m_T - m_0$ for different centralities for $K^{*0} + \bar{K}^{*0}$ as well as for peripheral collisions for $K^{*+} + \bar{K}^{*-}$ in Au+Au collisions at a cms energy of $\sqrt{s_{NN}} = 200$ GeV. The symbols show data from the STAR experiment while the solid lines show results from the PHSD calculations. For the $K^{*0} + \bar{K}^{*0}$ STAR data the legend is as follows: the solid black circles show data from central Au+Au collisions, the open stars show data for [0, 10]% central collisions, the open black squares show data for [30, 50]% central collisions and the open black circles show data for [50, 80]% central collisions. For the $K^{*+} + \bar{K}^{*-}$ STAR data the upside down solid black triangles show data for [50, 80]% central collisions. For the $K^{*0} + \bar{K}^{*0}$ PHSD results the legend is as follows: the solid red line shows results from central Au+Au collisions, the dashed olive line shows results for [0, 10]% central collisions, the dotted green line shows results for [30, 50]% central collisions and the dashed blue line shows results for [50, 80]% central collisions. For the $K^{*+} + \bar{K}^{*-}$ PHSD results the solid light blue line shows results for [50, 80]% central collisions. The STAR data are taken from [7, 8].

As can be seen in Fig. 14 the experimental data have also been taken for Au+Au collisions at a cms energy of

$\sqrt{s_{NN}} = 200$ GeV for different centralities. We have used the same K^* reconstruction procedure to calculate the reconstructed m_T spectrum of the K^* from PHSD simulations for the same centrality classes. The experimental data can be reproduced by the results from PHSD very well, separately for the different centralities. We note that the same restrictions and effects are also present at higher impact parameters. Rescattering and absorption effects play a role at central as well as at peripheral collisions and the cuts imposed on the reconstructed $K\pi$ pairs also lead to a lowering of the spectrum at small transverse mass.

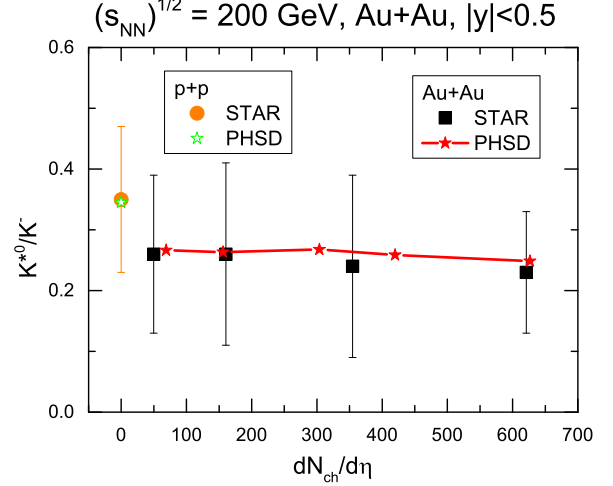


FIG. 15: The K^{*0}/K^- ratio versus $dN_{ch}/d\eta$ for Au+Au collisions at a cms energy of $\sqrt{s_{NN}} = 200$ GeV. The solid black squares show data from the Au+Au collision at the STAR experiment while the orange circle shows data from p+p collisions at STAR. The solid red stars show results from Au+Au PHSD calculations and the open green star shows results from p+p PHSD calculations. The STAR data are taken from [7, 9].

In Figs. 15 and 16 we show the ratios between K^{*0} and K^- as a function of the charged particle pseudorapidity and the cms energy, respectively, in comparison to the STAR data. The reason to study this particular ratio is that the quark content of K^* s and K is the same, the difference lies in the mass and the relative orientation of the quark spin. By studying this ratio one hoped to find out more about the K^* production properties and the freeze-out conditions in relativistic heavy-ion collisions. The PHSD results in Fig. 15 reproduce STAR data very well within error bars which indicates the production channels in PHSD are in line with the experimental observation.

The ratios in Fig. 15 are shown as the real ratios, i.e. they have not been normalised to the ratio measured in minimum bias p+p collisions, as was done in [7]. We obtain a similar value for the K^{*0} to K^- ratio in p+p collisions as in the experiment. Furthermore, the PHSD results match the experimental data from Ref. [7] as well. Furthermore, from Fig. 15 one can see that there

is almost no dependence of the K^{*0}/K^- ratio on the centrality and accordingly the impact parameter.

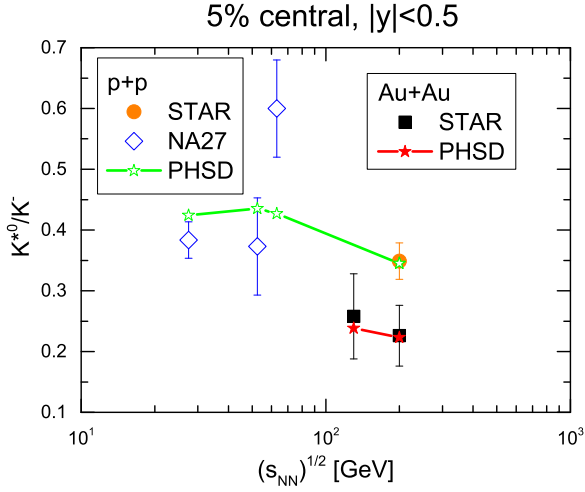


FIG. 16: The K^{*0}/K^- ratio as a function of the cms energy $\sqrt{s_{NN}}$. The black squares show data from Au+Au collisions at the STAR experiment. The orange circle shows STAR data from p+p collisions. Additionally data from the NA27 experiment is shown for lower cms energies as open blue diamonds. The red and green symbols show results from a PHSD calculation. The solid red stars show results for Au+Au collisions while the open green stars show results for p+p collisions. The STAR data are taken from [7, 8].

Fig. 16 shows the same ratio as a function of different cms energies. One has to note that we show Au+Au and p+p data in accordance with the original publication where this data have appeared. As seen the PHSD results can reproduce these STAR data within error bars well, too. There seems to be no strong dependence of the ratio with cms energy.

Figs. 17 and 18, furthermore, show the average transverse momentum as a function of the charged particle pseudorapidity and the average number of participants, respectively. Again, the average transverse momentum results from PHSD agree with the data from the STAR experiment very well, both for p+p and also for Au+Au collisions.

Furthermore, in Fig. 18 one can see that our results agree with the data for peripheral collisions, with only few participating nucleons, and for central collisions where the number of participants is high. The STAR Collaboration has found that the average transverse momentum of the K^* s is higher than the average transverse momentum of kaons and pions. This might indicate that the average transverse momentum is more strongly related to the mass of the particle observed.

So far, most of the collisions were performed for Au+Au or p+p collisions. However, there are also data Au+Cu which have been provided in form of the average transverse momentum in Fig. 19. The data are available for a cms energy of $\sqrt{s_{NN}} = 200$ GeV and for a lower

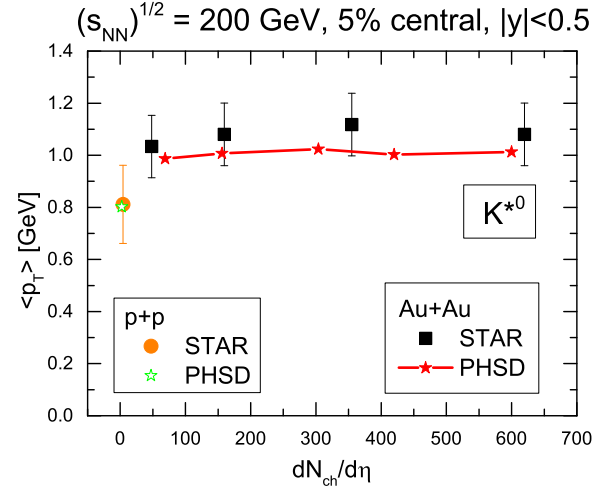


FIG. 17: The average transverse momentum $\langle p_T \rangle$ as a function of $dN_{ch}/d\eta$. The black and orange symbols show data for K^{*0} from the STAR experiment. The solid black squares show data for Au+Au collisions while the solid orange circle shows data for p+p collisions. The green and red symbols show results for K^{*0} from a PHSD simulation. The solid red stars show results for Au+Au collisions while the open green star shows results for p+p collisions. The STAR data are taken from Ref. [7].

energy of $\sqrt{s_{NN}} = 62.4$ GeV. In Fig. 19 one can see that the results from PHSD reproduce the STAR data for Cu+Cu collisions also very well. Our average momentum for the reconstructed K^{*0} s as a function of the average number of participants agrees very well both for the higher energy of $\sqrt{s_{NN}} = 200$ GeV and also for lower energy of $\sqrt{s_{NN}} = 62.4$ GeV.

Finally, Fig. 20 shows experimental data and PHSD results for the elliptic flow v_2 , which is defined as the second harmonic coefficient of the Fourier expansion of the azimuthal particle distributions in momentum space

$$E \frac{d^3 N}{d^3 \vec{p}} = \frac{1}{2\pi} \frac{d^2 N}{p_T dp_T dy} \left(1 + 2 \sum_{n=1}^{\infty} v_n \cos(n(\phi - \Psi_R)) \right) \quad (10)$$

which we have taken as

$$v_2 = \frac{p_x + p_y}{p_x - p_y} \quad (11)$$

since the reaction plane is fixed in PHSD. In this figure the STAR data are taken from two different runs at RHIC. When considering the error bars of the experimental data from the first (RunII) and the second (RunIV) both data are in agreement and a significant non-zero v_2 for the K^{*0} can be extracted in minimum bias Au+Au collisions at a cms energy of $\sqrt{s_{NN}} = 200$ GeV. Again within error bars the PHSD results are compatible with the measurements.

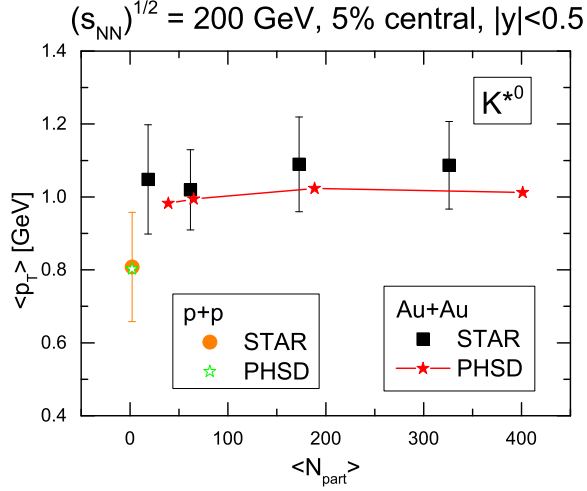


FIG. 18: The average transverse momentum $\langle p_T \rangle$ versus the average number of participants $\langle N_{part} \rangle$. The black and orange symbols show data for K^{*0} from the STAR experiment. The solid black squares show data for Au+Au collisions while the solid orange circle shows data for p+p collisions. The green and red symbols show results for K^{*0} from a PHSD simulation. The solid red stars show results for Au+Au collisions while the open green star shows results for p+p collisions. The STAR data are taken from Ref. [8].

VI. SUMMARY

In this study we have investigated the strange vector meson (K^* , \bar{K}^*) dynamics in heavy-ion collisions based on the microscopic off-shell PHSD transport approach which incorporates partonic and hadronic degrees-of-freedom and includes a crossover phase transition from partons to hadrons and vice versa. We have studied the influence of in-medium effects on the strange resonance dynamics by implementing the in-medium K^* , \bar{K}^* spectral functions for the production of strange vector mesons by hadronic channels as well as by hadronization of strange and light quarks. For that we employed the results of our previous study in Ref. [29] where we obtained the self-energies for the K^* and \bar{K}^* from a self-consistent coupled-channel chiral unitary G-Matrix approach. The full G-matrix result we have approximated in terms of relativistic Breit-Wigner spectral functions which are easy to incorporate in the off-shell PHSD transport approach. The real and imaginary parts of these self-energies are related to a mass shift and collisional broadening of the spectral functions. Furthermore, the decay width of the spectral function was calculated using the in-medium spectral functions of the K and \bar{K} on the K^* and \bar{K}^* decays, respectively.

We mention that the PHSD approach treats the partonic stage on a microscopic basis and accounts for the dynamical hadronization of quarks based on transition rates from the DQPM model. This allows to investigate the properties of the K^* mesons produced from the QGP

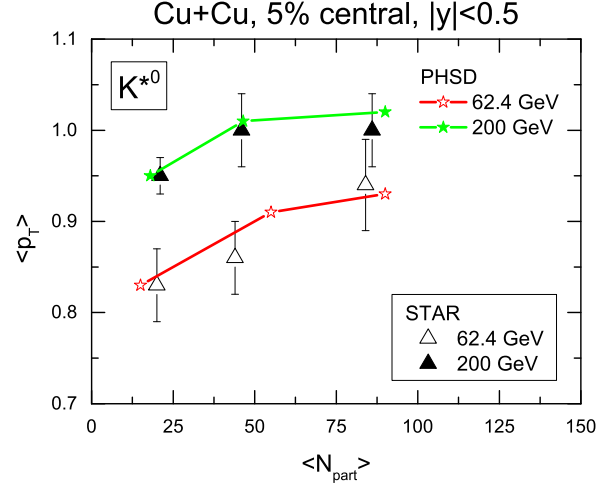


FIG. 19: The average transverse momentum $\langle p_T \rangle$ as a function of the average number of participants $\langle N_{part} \rangle$ for Cu+Cu collisions at different energies. The open and solid black triangles show K^{*0} from the STAR experiment for $\sqrt{s_{NN}} = 62.4$ GeV and for $\sqrt{s_{NN}} = 200$ GeV respectively. The open red and solid green stars show results for K^{*0} s from a PHSD simulations from reconstructed K and π pairs for $\sqrt{s_{NN}} = 62.4$ GeV and for $\sqrt{s_{NN}} = 200$ GeV respectively. The STAR data are taken from Ref. [8].

by hadronization without assumptions on "freeze-out" criteria as used in hydrodynamic descriptions of heavy-ion collisions. Moreover, even after hadronization in some area of the expanding fireball the K^* mesons can enter other "hot spots" or blobs of QGP and dissolve to quarks and antiquarks again and vice versa.

We have confronted the results of our microscopic calculations with the experimental data at RHIC energies and used reconstruction methods in close analogy to the experimental ones - by looking at the decay products of K^* mesons to pions and kaons $K^* \rightarrow K + \pi$ and compare to the real spectra of all K^* formed in A+A collisions. By that we could pin down the influence of final-state interactions of the decay products and quantify the distortion of the 'true' signal in heavy-ion collisions. As a 'reference frame' for a check of our model we used the experimental data for pp collisions and found a good agreement between the PHSD calculations and data.

Our findings can be summarized as follows:

- The fraction of K^* mesons produced by hadronization from the QGP in the final observables is relatively small compared to the hadronic production channels.
- Most of the final K^* 's stem from the hadronic phase, i.e dominantly from pion-kaon annihilation ($K + \pi \rightarrow K^*$).
- The decay products of the K^* mesons - final pions and kaons - suffer from partly resonant final state

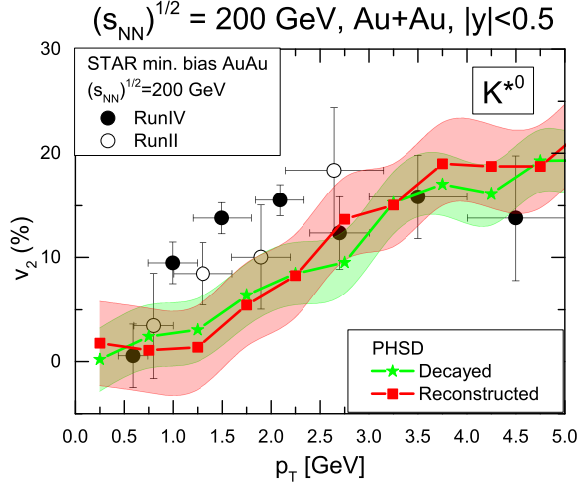


FIG. 20: The elliptic flow v_2 as a function of the transverse momentum p_T . The open and solid black circles show data from Run II and Run IV of the STAR experiment respectively. The runs were done for K^{*0} in minimum bias Au+Au collisions at a cms energy of $\sqrt{s_{NN}} = 200$ GeV. The solid green stars and solid red squares show results from a PHSD simulation. The solid green stars show the K^{*0} v_2 for K^{*0} s directly at their decay point while the red solid squares show v_2 for K^{*0} s which have been reconstructed from the final K s and π s. The STAR data are taken from Ref. [7, 9].

interactions which lead to a significant distortion of the K^* spectra. The low transverse momentum p_T part is most sensitive to these 'losses' of kaon-pion correlations while the high p_T K^* mesons are less affected. That is in line with the conclusions from the previous studies [20–22].

- At RHIC energies most of the K^* 's are produced at relatively low baryon densities due to the rapid expansion of the fireball, thus in-medium effects in the hadronic phase are small at these energies. With decreasing beam energy, the fraction of the hadronic phase and its duration increases, which leads to the fact that the K^* mesons probe much high baryon densities. In this respect the future FAIR and NICA facilities are optimally set up to

study in-medium K^* resonance dynamics.

- The differences in the slope of the p_T spectra from various channels is small (cf. Fig. 10) which makes it difficult to distinguish experimentally the "origin" of K^* mesons by applying different cuts e.g. on transverse momentum.
- The restriction of the invariant mass region for the possible reconstructed K^* s leads to a further sizeable distortion of the K^* signal and artificially enhance the effective slope parameter of the p_T or m_T spectrum.
- The number of K^* s that can be reconstructed from final pions and kaons is heavily reduced in comparison to the number of K^* s that have been produced during a heavy-ion collisions; especially it applies to the K^* 's produced and decayed at the early stages of heavy-ion collision, whereas the number of reconstructable K^* s in the later stages is much closer to the number of K^* s that have been produced due to the fact that the system expands rapidly and the final state interaction is less probable.

Furthermore, we mention that the dominance of final hadronic channels in the strange vector-meson channel is in line with our findings for the dilepton production from non-strange ρ and ω decays in these reactions [2].

Acknowledgements

The authors acknowledge inspiring discussions with Jörg Aichelin, Wolfgang Cassing, Taesoo Song, Pierre Moreau, Anders Knospe, Laura Tolos and Vadim Voronyuk. A.I. acknowledges support by HIC for FAIR and HGS-HiRe for FAIR. D.C. acknowledges support by Ministerio de Economía y Competitividad (Spain), Grant Nr. FIS2014-51948-C2-1-P. This work was supported by BMBF and HIC for FAIR. The computational resources have been provided by LOEWE-CSC at the Goethe University Frankfurt. This work was supported by U.S. Department of Energy Office of Science under contract number DE-SC0003892.

-
- [1] Proceedings of Quark Matter-2014, Nucl. Phys. A **931**, 1 (2014).
 - [2] O. Linnyk, E. L. Bratkovskaya, W. Cassing, Prog. Part. Nucl. Phys. **87** (2016) 50
 - [3] A. Adare et al. (PHENIX Collaboration), Phys. Rev. Lett. **98**, 172301 (2007); B. Abelev et al. [ALICE Collaboration], JHEP **1209**, 112 (2012).
 - [4] J. Rafelski, J. Letessier and G. Torrieri, Phys. Rev. C **64** (2001) 054907 Erratum: [Phys. Rev. C **65** (2002) 069902]
 - [5] C. Markert, G. Torrieri and J. Rafelski, AIP Conf. Proc. **631**, 533 (2002)
 - [6] C. Markert, R. Bellwied and I. Vitev, Phys. Lett. B **669** (2008) 92
 - [7] J. Adams et al. [STAR Collaboration], Phys. Rev. C **71** (2005) 064902
 - [8] M. M. Aggarwal et al. [STAR Collaboration], Phys. Rev. C **84** (2011) 034909
 - [9] L. Kumar [STAR Collaboration], EPJ Web Conf. **97** (2015) 00017
 - [10] B. B. Abelev et al. [ALICE Collaboration], Phys. Rev. C **91** (2015) 024609
 - [11] M. Bando, T. Kugo and K. Yamawaki, Nucl. Phys. B

- 259** (1985) 493.
- [12] E. Oset and A. Ramos, Eur. Phys. J. A **44** (2010) 445.
 - [13] E. Oset, A. Ramos, E. J. Garzon, R. Molina, L. Tolos, C. W. Xiao, J. J. Wu and B. S. Zou, Int. J. Mod. Phys. E **21** (2012) 1230011.
 - [14] M. Bando, T. Kugo, S. Uehara, K. Yamawaki and T. Yanagida, Phys. Rev. Lett. **54** (1985) 1215.
 - [15] M. Bando, T. Kugo and K. Yamawaki, Phys. Rept. **164** (1988) 217.
 - [16] M. Harada and K. Yamawaki, Phys. Rept. **381** (2003) 1
 - [17] U. G. Meissner, Phys. Rept. **161** (1988) 213.
 - [18] E.L. Bratkovskaya, J. Aichelin, M. Thomere, S. Vogel, M. Bleicher, Phys. Rev. C **87** (2013) 064907
 - [19] W. Cassing, L. Tolós, E. L. Bratkovskaya, A. Ramos, Nucl. Phys. A **727** (2003) 59
 - [20] M. Bleicher and J. Aichelin, Phys. Lett. B **530** (2002) 81
 - [21] S. Vogel, J. Aichelin and M. Bleicher, J. Phys. G **37** (2010) 094046
 - [22] A. G. Knospe, C. Markert, K. Werner, J. Steinheimer and M. Bleicher, Phys. Rev. C **93** (2016) no.1, 014911
 - [23] M. Lutz, Phys. Lett. B **426** (1998) 12
 - [24] A. Ramos and E. Oset, Nucl. Phys. A **671** (2000) 481
 - [25] L. Tolos, A. Ramos, A. Polls and T. T. S. Kuo, Nucl. Phys. A **690** (2001) 547
 - [26] L. Tolos, A. Ramos and E. Oset, Phys. Rev. C **74** (2006) 015203
 - [27] M. F. M. Lutz, C. L. Korpa and M. Moller, Nucl. Phys. A **808** (2008) 124
 - [28] L. Tolos, D. Cabrera and A. Ramos, Phys. Rev. C **78** (2008) 045205
 - [29] A. Ilnert, D. Cabrera, P. Srisawad and E. Bratkovskaya, Nucl. Phys. A **927** (2014) 249
 - [30] W. Cassing and E. L. Bratkovskaya, Nucl. Phys. A **831** (2009) 215
 - [31] E. L. Bratkovskaya, W. Cassing, V. P. Konchakovski and O. Linnyk, Nucl. Phys. A **856** (2011) 162
 - [32] L. P. Kadanoff and G. Baym, *Quantum Statistical Mechanics*, Benjamin, New York, 1962.
 - [33] S. Juchem, W. Cassing and C. Greiner, Nucl. Phys. A **743** (2004) 92
 - [34] W. Cassing, Nucl. Phys. A **795** (2007) 70
 - [35] W. Ehehalt and W. Cassing, Nucl. Phys. A **602** (1996) 449.
 - [36] W. Cassing and E. L. Bratkovskaya, Phys. Rept. **308** (1999) 65.
 - [37] B. Nilsson-Almqvist and E. Stenlund, Comp. Phys. Comm. **43**, 387 (1987); B. Andersson, G. Gustafson, and H. Pi, Z. Phys. C **57**, 485 (1993).
 - [38] W. Cassing, Nucl. Phys. A **791** (2007) 365
 - [39] Y. Aoki, S. Borsanyi, S. Durr, Z. Fodor, S. D. Katz, S. Krieg and K. K. Szabo, JHEP **0906** (2009) 088
 - [40] M. Cheng *et al.*, Phys. Rev. D **77** (2008) 014511
 - [41] B. Andersson, G. Gustafson and H. Pi, Z. Phys. C **57** (1993) 485.
 - [42] W. Cassing, Eur. Phys. J. ST **168** (2009) 3
 - [43] S. Borsanyi *et al.*, Phys. Rev. D **92** (2015) no.1, 014505
 - [44] L. Tolos, R. Molina, E. Oset and A. Ramos, Phys. Rev. C **82** (2010) 045210
 - [45] D. Gamermann, C. Garcia-Recio, J. Nieves and L. L. Salcedo, Phys. Rev. D **84** (2011) 056017
 - [46] A. Ramos, L. Tolos, R. Molina and E. Oset, Eur. Phys. J. A **49** (2013) 148
 - [47] K. A. Brueckner, Phys. Rev. **97** (1955) 1353.
 - [48] J. Beringer *et al.* [Particle Data Group Collaboration], Phys. Rev. D **86** (2012) 010001.
 - [49] E. Oset and A. Ramos, Nucl. Phys. A **635** (1998) 99
 - [50] N. Kaiser, P. B. Siegel and W. Weise, Nucl. Phys. A **594** (1995) 325
 - [51] E. L. Bratkovskaya and W. Cassing, Nucl. Phys. A **807** (2008) 214
 - [52] S. Cho, S.H. Lee arXiv:1509.04092
 - [53] R. Shahoyan [NA60 Collaboration], Nucl. Phys. A **827** (2009) 353C.